

## Supplementary Information

### Highly robust aluminum counter cation-based monophosphate tungsten bronze novel electro-catalysts for oxygen evolution in acidic solution

Md. Imran Hossain<sup>a</sup>, Tapas Debnath<sup>b</sup>, M. Yousuf Ali Mollah<sup>a</sup>, Md. Abu Bin Hasan Susan<sup>a</sup> and Md. Mominul Islam<sup>a\*</sup>

<sup>a</sup>Department of Chemistry, Faculty of Science, University of Dhaka, Dhaka 1000, Bangladesh

<sup>b</sup>Department of Theoretical and Computational Chemistry, Faculty of Science, University of Dhaka, Dhaka, Bangladesh

\*For correspondence: E-mail: mominul@du.ac.bd

#### Material synthesis.

MPTBs were synthesized by solution combustion synthesis which involves uniform reaction solution preheating prior to self-ignition. Typically, an appropriate amount of H<sub>2</sub>WO<sub>4</sub> and metal nitrate were dissolved in a minimum amount of aqueous ammonia. Glycerin and NH<sub>4</sub>H<sub>2</sub>PO<sub>4</sub> were added in a ratio of 1:8 in all experiment, here glycerin and ammonium dihydrogen phosphate acted as a fuel and oxidizer, respectively. Reactants were taken in an appropriate molar ratio according to equations S1-3.



The mixtures were carefully (temperature  $\leq 100$  °C) evaporated to viscous gel and prevented premature ignition. The gel was burned on a burner in a fume cupboard until evolution of gaseous substances such as N<sub>2</sub>, CO<sub>2</sub> and water vapor; the evolution of these substances led to the formation of the fluffy mass. The fluffy mass was grounded in an agate mortar to get the fine powder and then placed in a ceramic crucible. The fine powder was calcined in a tube furnace at temperature in ranges of 500 to 900 °C. Two heating atmospheres were chosen for the calcination of MPTB: one was calcined in presence of O<sub>2</sub> gas and another one in presence of N<sub>2</sub> gas in a tube furnace under a constant pressure 5 psi and with a flow rate of 100 L/h. By

following these methods, ten MPTBs formed with aluminum, chromium and iron counter-cations were synthesized at different temperatures. Cutty sark, sage and de york colored powder of Al-, Cr- and Fe-based MPTBs, respectively, were stored for further analyses and used as catalysts for OER. It is mentioning that the cutty sark color of Al-based MPTBs kept in open environment was found to remain unchanged even after more than one year. The conditions of synthesis of MPTBs with their abbreviated names are summarized in Table S1 below:

**Table S1.** Conditions of synthesis of MPTB catalysts

MPTB catalysts	Abbreviated name	<sup>a</sup> Calcination temperature (°C)
Al-series	AlO5	500
	AlO6	600
	AlO7	700
	AlN7	700
	AlO8	800
	AlO9	900
Fe-series	FeO7	700
	FeO8	800
Cr-series	CrO7	700
	CrO8	800

<sup>a</sup>Calcinations were carried out in O<sub>2</sub> atmosphere except for AlN7 that was calcined in N<sub>2</sub> atmosphere.

#### **Fourier-transform infrared spectroscopy.**

Vibrational spectra of the samples studied were recorded with Fourier-transform infrared (FTIR) spectrophotometer (Perkin Elmer, USA, Frontier FT-IR/NIR) in the range of 400–4000 cm<sup>-1</sup>. FTIR measurement of the sample was carried out in a KBr pellet by taking the weight ratio of a particular sample and KBr of around 0.005. For example, about 200 mg KBr and ~1-2 mg of solid powdered sample were mixed, grinded homogeneously and pressed to make a pellet. Background correction was done with a pure KBr pellet to avoid the contribution of infrared active atmospheric gases such as CO<sub>2</sub> and H<sub>2</sub>O vapor in the spectra.

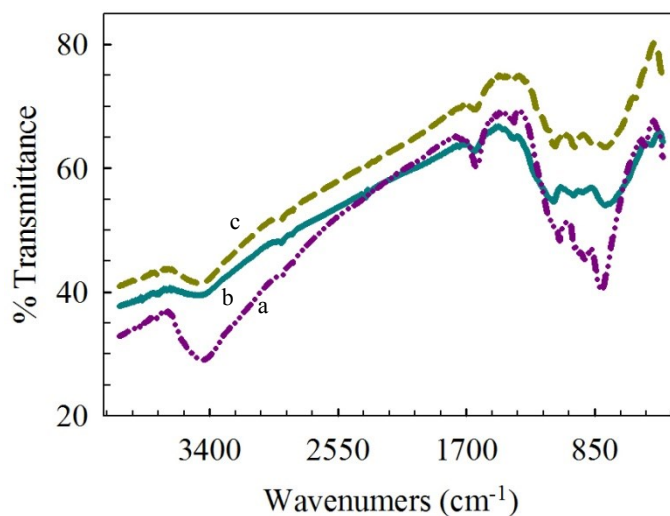


**Fig. S1.** FTIR spectra of (a) CrO7, (b) AlO7 and (c) FeO8.

The structure of MPTBs is composed of two types of polyhydrons such as octahedron and tetrahedron. The central metal, W resides in the octahedral site formed with  $O^{2-}$  anion; additionally the octahedral sites can be occupied by the counter-cations such as  $Al^{3+}$ ,  $Cr^{3+}$  and  $Fe^{3+}$ , whereas the tetrahedron are formed by the  $PO_4^{3-}$  group that actually act as conducting linkage between the sites formed via metal-oxygen bonding.<sup>S1</sup> The stretching vibration of Al-O at  $1100\text{ cm}^{-1}$  and XPS analysis (Fig. SI7) of Al  $2p$  ( $73.5\text{ eV}$ ) confirm the successful incorporation of  $Al^{3+}$  in AlO7.<sup>S2</sup> The band at  $1006\text{ cm}^{-1}$  is attributed to P-O asymmetric stretching vibration of phosphate group.<sup>S3</sup> Stretching and bending vibration modes of surface water molecules are found at  $3450$  and  $1645\text{ cm}^{-1}$ .<sup>S4</sup> Furthermore, the stretching vibration of Fe-O occurred at  $624\text{ cm}^{-1}$  confirms the presence of  $Fe^{3+}$  in FeO8 and the intense peak found at  $802\text{ cm}^{-1}$  is attributed to the presence of Cr-O species in CrO7.<sup>S4</sup>

### Scanning electron microscopy.

Scanning electron microscopy (SEM) was employed (Model: JEOL, JSM-6490LA, USA) to measure the morphology of synthesized MPTBs. The acceleration voltage of the electron gun was  $20\text{ kV}$  with a probe current of  $1.0\text{ nA}$ . Computer adapted software (ImageJ 1.51k, Java 1.6.0-24 (64-bit), USA) was used to measure the perimeter, circularity, solidity and number of nanosized particles in the SEM images of MPTB at defined scale. All of the originals images representing the morphologies of three series of MPTBs and the corresponding

mapping images are shown in Figs. S2 and S3. Moreover, the different parameters of the MPTBs particles determined using ImageJ software are compared in Table S2.

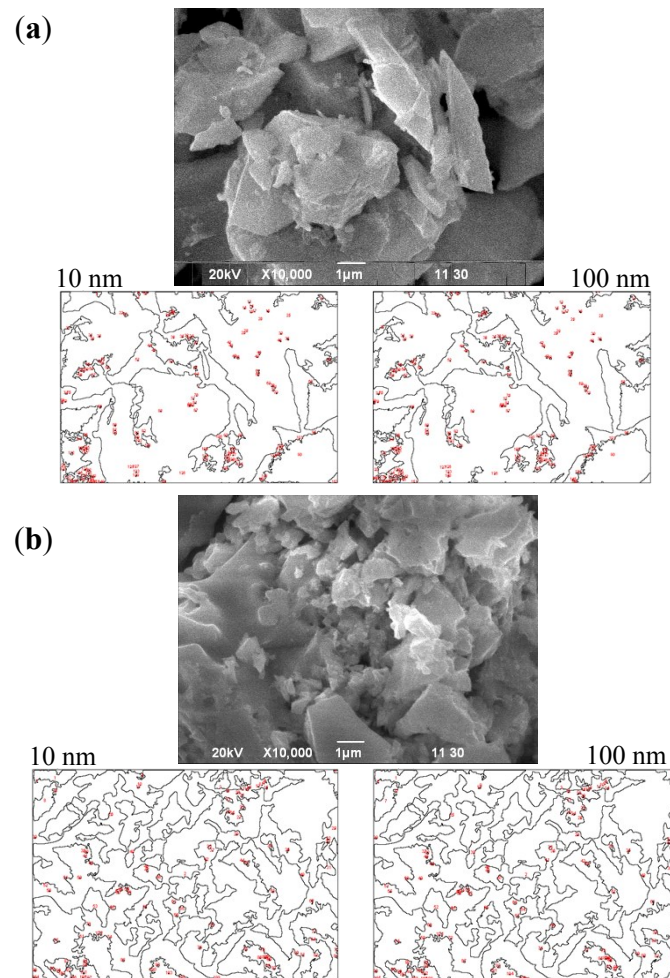


**Fig. S2.** SEM image of (a) AIO6 and (b) AIO7, these images were used to calculate the number of nanosized particles in the scales of 10 and 100 nm (red points are the locations of particles).

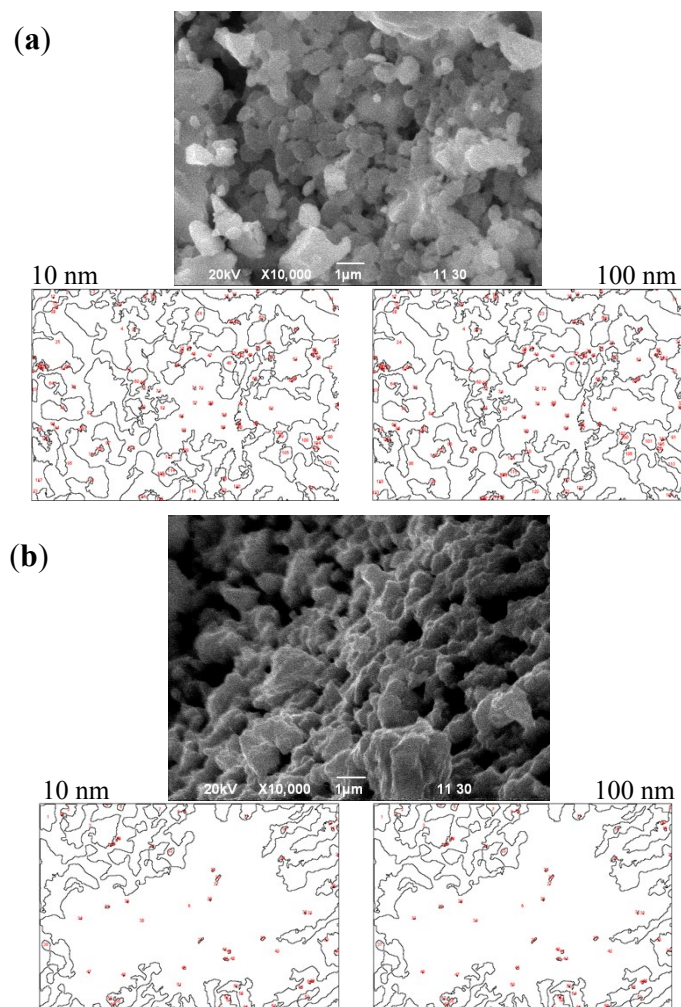


**Fig. S3.** SEM image of (a) AlN7 and (b) FeO8 were used to calculate the number of nanosized particles in the scales of 10 and 100 nm.

**Table S2.** Derived data of the SEM images of the MPTB catalysts

Abbreviated name	Defined scale (nm)	No. of particles (counts)	Perimeter (nm)	Circularity (out of 1)	Solidity (out of 1)
AlO6	10	152	84.7	0.877	0.884
	100	151	86.3	0.880	0.884
AlO7	10	109	169.4	0.852	0.878
	100	110	168.4	0.857	0.882
AlN7	10	125	145.1	0.776	0.845
	100	128	140.6	0.784	0.847
FeO8	10	63	186.0	0.806	0.869
	100	62	189.6	0.804	0.868

### Reflectance spectrophotometry.

Reflectance spectra were recorded using a double beam UV-visible spectrophotometer (Model: UV-1800, Shimadzu, Japan) with an integrating sphere attachment DRA-CA-30I to determine the optical band gap ( $E_g$ ) of the samples. According to the UV-vis spectral analysis (absorption or reflectance) as well as the type of transition band considered, directly or indirectly, the  $E_g$  value can be differed strongly from the method employed.<sup>S5- S7</sup> Among the optical methods, UV-vis diffuse reflectance spectroscopy is one of the most employed techniques.<sup>S8</sup> This characterization technique describes the electronic behavior present in the structure of the solid. Experimental  $E_g$  values were determined by using Kubelka–Munk method that is based on the following equation (S4):<sup>S9</sup>

$$f(R) = \frac{(1 - R)^2}{2R} \quad (S4)$$

where  $R$  is the reflectance and  $f(R)$  is proportional to the absorption coefficient ( $\alpha$ ). A modified Kubelka–Munk function can be obtained by multiplying the  $f(R)$  function by  $h\nu$ , using the corresponding coefficient ( $m$ ) associated with an electronic transition as follows:

$$(f(R) \times h\nu) = B (h\nu - E_g)^m \quad (S5)$$

For direct and indirect allowed transition  $m = \frac{1}{2}$  and 2, respectively and  $B$  is an energy-independent constant. By plotting the equation (S5) as a function of the energy ( $h\nu$ ) in eV, the  $E_g$  of the samples can be obtained and this is known as the Tauc method.<sup>S10, S11</sup> The optical  $E_g$  was determined by extrapolating the linear portion of the plot to  $(\alpha h\nu)^m = 0$ .

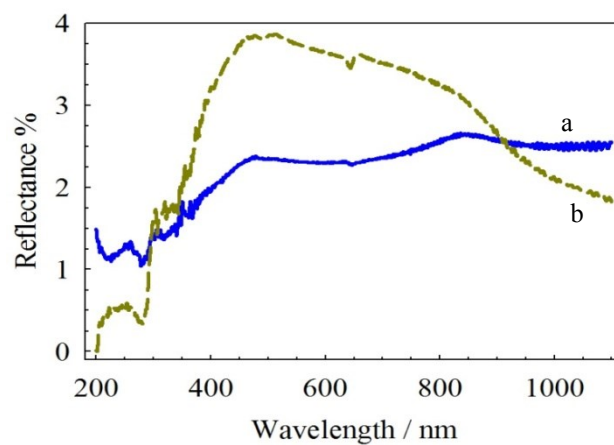
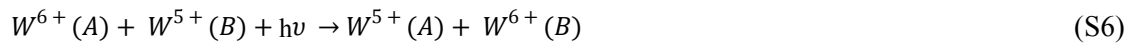


**Fig. S4.** The reflectance spectra of (a) AlO7 and (b) AlN7.

The absorbance at near infrared region of AlN7 is large which are due to the vibrational and rotational motions of the molecule (Fig. S4). High % reflectance at the visible region of AlN7 is due to the large number of scattering center and the intense peak at UV region confirms the presence of  $W^{5+}$  and  $W^{6+}$ , wherein the following process<sup>S12</sup> will be responsible for the absorption of UV light (Eq. S6). AlO7 does not show similar characteristic at near infrared and visible region and the percentage of  $W^{5+}$  is higher than  $W^{6+}$  (Fig. S7), so the following process cannot be favorable for the absorption of UV light.<sup>S12</sup>



However, the values of  $E_g$  for AlO7 and AlO7 are summarized in Table S3. The band gap calculated by Tauc method (indirect  $E_g$ ) lies close to the respective value obtained from the derivation of absorption spectrum fitting (DASF) method<sup>S13</sup> for AlO7 and AlN7.

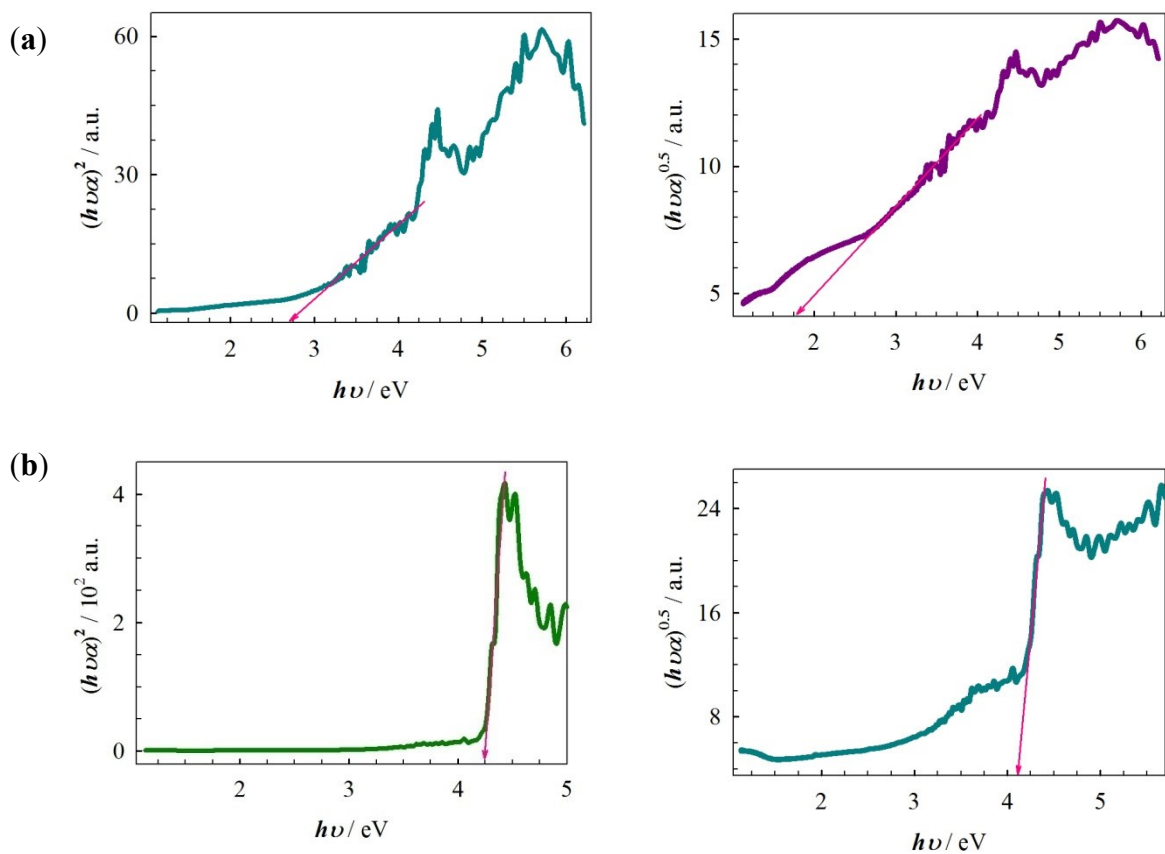


**Fig. S5.** Tauc plot of (a) AlO7 and (b) AlN7 assuming direct (left) and indirect (right) transitions. The lines with arrow show the respective intercepts for  $E_g$ .

**Table S3.** Calculated value of  $E_g$  of AlO7 and AlN7

Sample	Tauc method		DASF method
	Direct	Indirect	
AlO7	2.70	1.77	1.58
AlN7	4.24	4.11	3.27

The DASF method is deduced as follows:

$$\ln\left[\frac{f(R)}{\lambda}\right] + \ln s = \ln[B(hc)^{m-1}] + m \ln\left(\frac{1}{\lambda} - \frac{1}{\lambda_g}\right) \quad (S7)$$

where  $\lambda$  is the wavelength,  $c$  is the velocity of light,  $\lambda_g$  is the wavelength corresponding to the optical band gap and  $s$  is the scattering coefficient.

Now, the equation (S7) can be simplified as:

$$\frac{d\left\{\ln\left[\frac{f(R)}{\lambda}\right]\right\}}{d\left(\frac{1}{\lambda}\right)} = \frac{m}{\frac{1}{\lambda} - \frac{1}{\lambda_g}} \quad (S8)$$

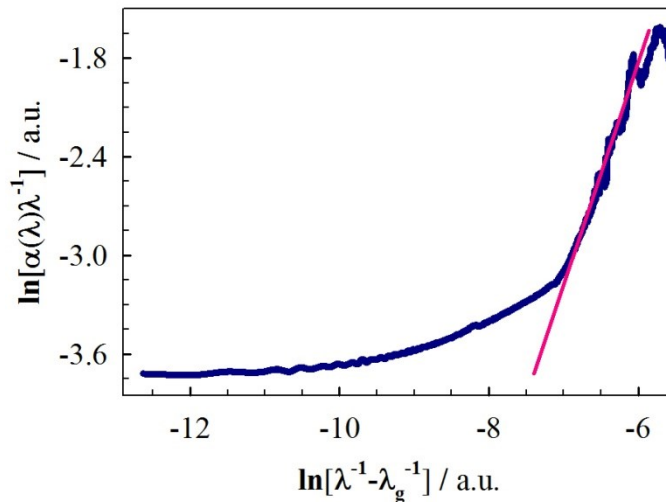


**Fig. S6.** Plot of  $\ln[\alpha(\lambda)\lambda^{-1}]$  versus  $\ln(\lambda^{-1} - \lambda_g^{-1})$  for the AlO7 sample.

The value of  $\lambda_g = 784$  nm (1.58 eV) is the wavelength of the band gap transition. The slope of the linear section of the plot shown in Fig. S16 is 1.19 ( $\approx 2$ ), indicating an indirect allowed band gap. Identical result was also found for AlN7. These  $E_g$  values are compared in Table S13 with those determined with so-called Tauc method as described above. The  $E_g$  values determined for an indirect band gap using both methods are consistent with each other. Thus, the band gap of the Al-series MPTBs is indirect in character.

### **X-ray photoelectron spectroscopy.**

X-ray photoelectron spectroscopy (XPS) was carried out using an Omicron EA 125 X-ray photoelectron spectrometer, which was equipped with a modified UHV chamber, by using MgK $\alpha$  (1253.6 eV) radiation.

XPS analysis confirms the presence of lowest amount of phosphate ( $\text{PO}_4^{3-}$ ) in AlO7 than the AlO6 and AlN7 (Fig. S8). The decreasing trend of  $\text{W}^{5+}$  and  $\text{W}^{6+}$  oxidation states is affiliated to the decomposition of  $\text{PO}_4^{3-}$  group with increment of temperature (Table S4). Furthermore, the inert ( $\text{N}_2$ ) atmosphere hindered such modification at 700 °C that is revealed through the XPS analysis of AlN7. Almost same percentage of  $\text{Al}^{3+}$  is found in AlO6 and AlN7 (Fig S7), but slightly high intensity is observed in AlO7 at around 73.5 eV. Other weak peaks are found at 70.5 and 69.2 eV for Al-series that were calcined at 600 and 700 °C. The observed shift of weak peak to lower binding energy signifies the stabilization of insulating domain.<sup>S14</sup> This effect is being prominent in AlO6 for the presence of  $\text{W}^{4+}$  and  $\text{W}^{5+}$  oxidation states (Table S4). Nonetheless, the peak at 70.5 eV appeared for AlO7 possesses higher intensity than AlN7 because of high content of  $\text{W}^{5+}$ . In addition, lower content of  $\text{O}^{2-}$  in AlO7 supports the better conductivity than the others.

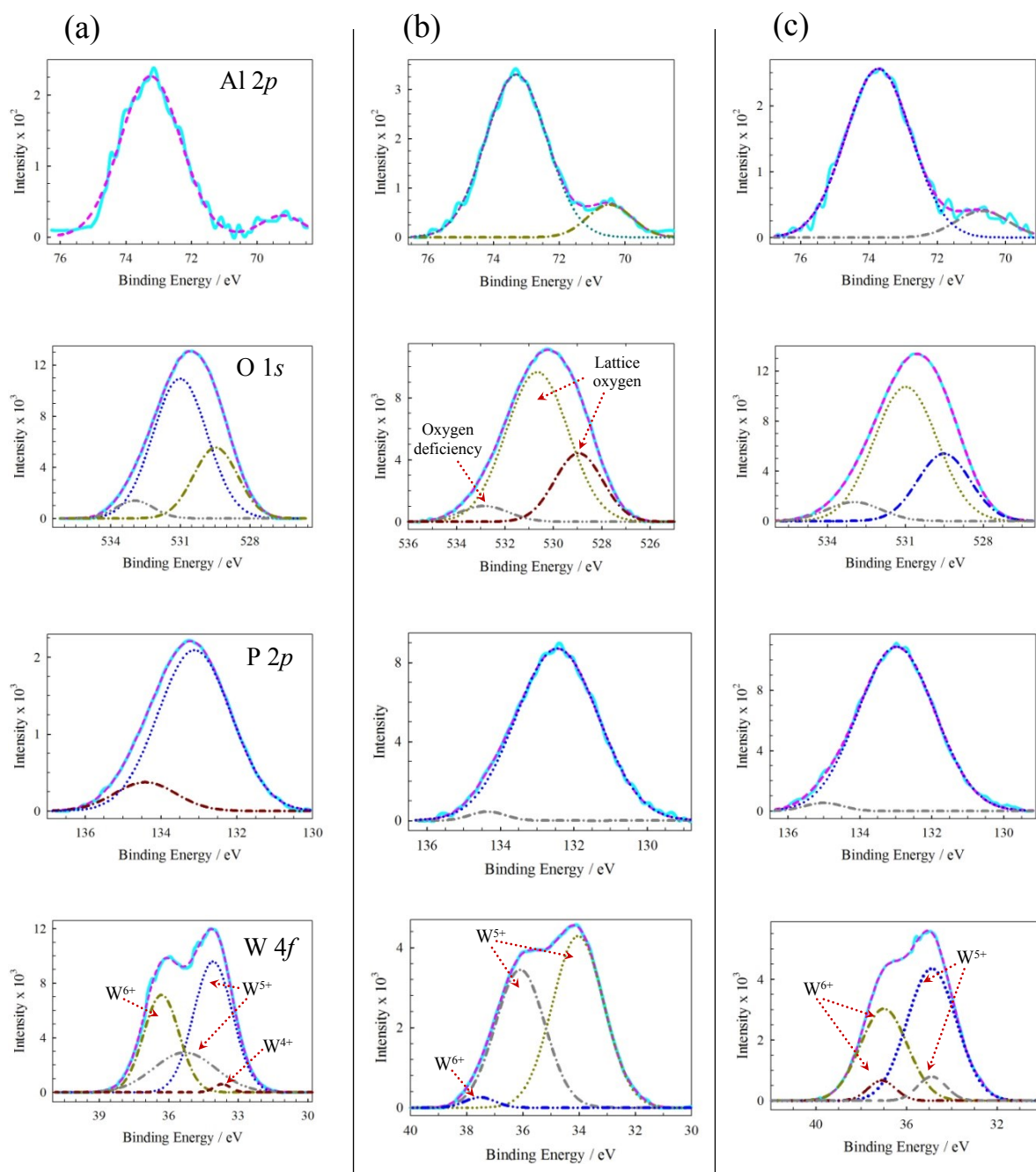


**Fig. S7.** XPS spectra of Al  $2p$ , O  $1s$ , P  $2p$  and W  $4f$  for (a) AlO6, (b) AlO7 and (c) AlN7.

**Table S4.** Derived data of different oxidation states of tungsten in Al-based MPTBs

Catalysts	#Area integration (%)		
	W <sup>4+</sup> state	W <sup>5+</sup> state	W <sup>6+</sup> state
AlO6	1	77	22
AlO7	-	98	2
AlN7	-	60	40

# Experimental XPS data are interpreted through the deconvolution (Fig. S7)

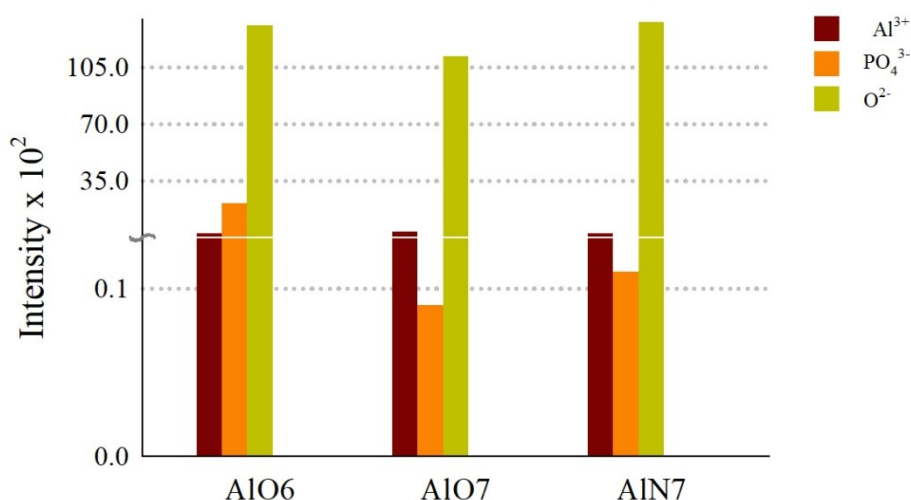


**Fig. S8.** Degree of different chemical entities in MPTB.

### X-ray powder diffraction.

X-ray powder diffraction (XRD) patterns of all the synthesized powder samples were recorded with a philips PW-1830 X-ray generator operating at 40 kV, 40 mA and XDC-700 Guinier Hagg focusing camera using Cu K $\alpha_1$  radiation ( $\lambda = 1.540598 \text{ \AA}$ ). X-ray was exposed for 15 min on an image plate for each sample. Image pate is a laser activated sheet which was scanned using HD-CD 35 NDT/CR 35 NDT scanner to get intensity versus line position (mm) pattern. The XRD pattern of intensity versus  $2\theta$  was found after conversion of line position from millimeter to  $2\theta$  from the geometry of camera and Bragg equation. The crystallite size ( $D$ ) of MPTB was calculated using Scherrer's Equation (S4):<sup>S15</sup>

$$D = \frac{0.9 \lambda}{\beta \cos \theta} \quad (\text{S9})$$

where  $\beta$  is full width at half maximum (FWHM in radian) of a peak,  $\theta$  is the angle in radian and  $\lambda$  is the wavelength (1.540598  $\text{\AA}$ ) of incident X-rays. XRD data are refined through match and endeavour software (version: 3.6.2.121 and 1.8b, Crystal Impact, Germany); systematic data are tabulated in Tables S5 and S6.

**Table S5.** Summary of data collection and crystal structure refinement of AlO7

Formula sum	Al <sub>8</sub> W <sub>40</sub> O <sub>192</sub> P <sub>24</sub>
Formula weight	11385.11
Crystal system	Orthorhombic
Space group	Pna2 <sub>1</sub> (no. 33)
<i>a</i> (Å)	17.1231
<i>b</i> (Å)	9.1463
<i>c</i> (Å)	7.5115
<i>Z</i>	2
Cell volume (Å <sup>3</sup> )	1176.40
Density (g/cm <sup>3</sup> )	ca. 16.070
Two body energy (eV/atom)	48.8151
R-factor (%)	54

**Table S6.** Assignment of XRD data of AlO7

<i>2θ</i> exp.	<i>2θ</i> calc.	<i>d</i> exp.	<i>d</i> calc.	<i>I</i> exp.	<i>h</i>	<i>k</i>	<i>l</i>
22.73	22.75	3.90917	3.90618	155.2	0	2	1
22.94	22.92	3.87368	3.87713	248.0	4	1	0
23.33	23.34	3.81059	3.80834	583.0	1	2	1
23.68	23.67	3.75445	3.75576	1000.0	0	0	2
33.38	33.18	2.68216	2.69761	395.5	4	1	2
33.56	33.57	2.66805	2.66779	566.6	6	0	1
41.59	41.40	2.16980	2.17920	149.4	5	3	1
48.74	48.46	1.86670	1.87706	153.9	8	2	1
54.95	54.92	1.66950	1.67042	187.5	7	4	0

Substantially high intensity of some high index facets such as [410] and [601] that are generally expected to offer a high catalytic activity<sup>S16</sup> were observed along with others facets in case of AlO7. On the other hand, there are two classes of layered solids: (i) those in which the sheets are uncharged and interact through van der Waals forces, such as, graphite and silicates (i.e. talc) and (ii) those in which charged sheets are held together by charge-balancing counter-ions including clays, layered perovskites, layered double hydroxides, layered PO<sub>4</sub><sup>3-</sup>, and numerous other ternary oxides that typically contain protons, alkali cations, or alkali earth cations between layers.<sup>S17</sup> AlO7 can be classified as second category

layered structure crystal, where  $\text{PO}_4^{3-}$  ions act as the connector between mixed metals layers. These two dimensional (2D) layered materials render high mobility as observed in the present case of AlO7 *vide infra*.

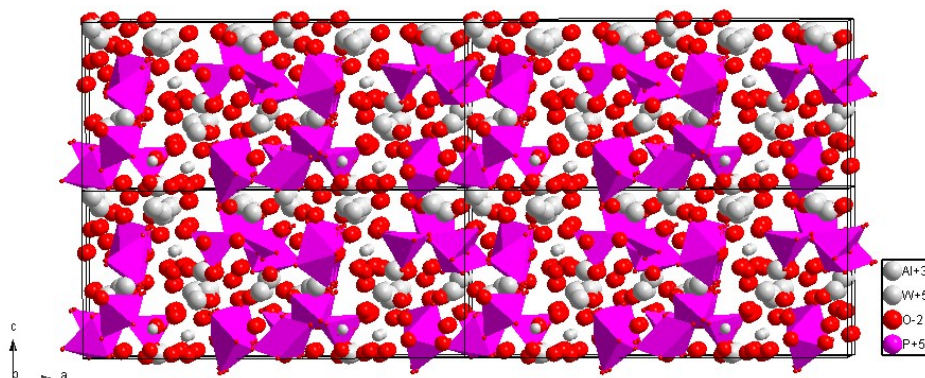


**Fig. S9** 2D-layered crystalline structure of AlO7.

### Electrochemical analysis of OER.

For investigating the catalytic activities towards OER, the MPTBs prepared were deposited on graphite disk electrode (diameter ca. 0.615 cm). The depositions of the catalysts were carried out by following solution casting method, where ethanol was used as the solvent and PVdF was the binder. The recipes of casting materials used are summarized in Table S7.

**Table S7.** Composition of mixture used for the fabrication of graphite electrode

MPTB sample	Sample taken (mg)	Binder PVdF (mg)
AlO5	5.2	0.7
AlO6	5.4	0.8
AlO7	4.3	0.7
AlN7	5.9	0.5
AlO8	4.6	0.6
AlO9	4.5	0.7
FeO7	6.1	0.8
FeO8	4.6	0.6
CrO7	4.8	0.7
CrO8	4.3	0.6

The electrochemical measurements were carried out using a silver | silver chloride | saturated KCl solution [Ag | AgCl | KCl (sat.)] electrode. For an easy understanding of formal energy involved with electrode reaction, it is convenient to refer the applied potential against normal hydrogen electrode (NHE) scale. Firstly, the conversion of overpotential in NHE scale is described below:

$$E_{\text{H}_2\text{O}/\text{O}_2} = (1.229 - 0.059 \text{ pH}) \text{ V vs. NHE} \quad (\text{S10})$$

$$= 1.182 \text{ V vs. NHE} \quad [\text{pH of } 0.08 \text{ M H}_2\text{SO}_4 \text{ is } 0.8]$$

$$E_{\text{NHE}} (\text{applied}) = (E_{\text{Ag} / \text{AgCl} / \text{KCl}} (\text{applied}) + 0.205) \text{ V} \quad (\text{S11})$$

$$\text{Overpotential, } \eta_a = E_{\text{NHE}} (\text{applied}) - 1.182 \text{ V vs. NHE} \quad (\text{S12})$$

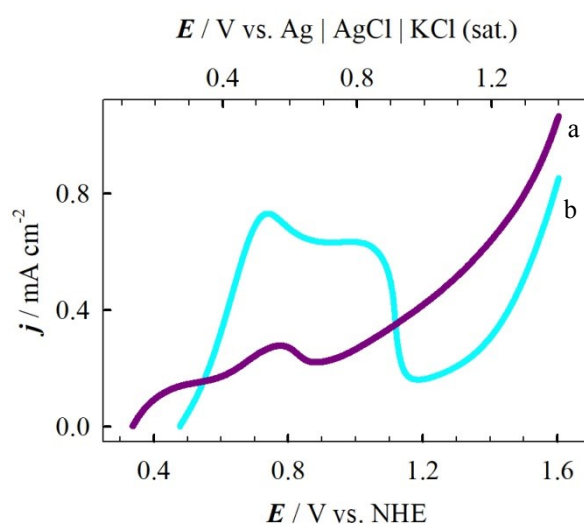


**Fig. S10.** LSVs of OER measured with (a) CrO8 and (b) FeO7-modified graphite electrodes in 0.08 M H<sub>2</sub>SO<sub>4</sub> solution at a potential scan rate of 5 mV/s.

Secondly, the conversion of  $\eta_a$  are well-exemplified in Fig. S10 of the linear sweep voltammograms (LSVs) measured for OER at CrO8 and FeO7 modified graphite electrodes in aqueous acidic solution. The shape of the LSV responses of OER measured at CrO8 and FeO7 differ from the corresponding MPTBs calculated at 700 and 800 °C, respectively. From the measured LSVs using all MPTBs synthesized the onset overpotential ( $\eta_{\text{onset}}$ ) was determined and these values are compared in Table S8.  $\eta_{\text{onset}}$  of AlO5 and AlO6 is

comparatively higher than those of the other Al-series MPTBs; AlO6 shows catalytic improvement towards OER than AlO5 (Table S8). Similarly, a drastic decrease in  $\eta_{\text{onset}}$  of 101 mV is observed between AlO6 and AlO7, but no significant change is noticed for AlO8 and AlO9. The  $\eta_{\text{onset}}$  values were found to negligibly increase in repeated uses of the electrodes prepared using Al-based MPTBs. On the contrary, the scenarios of catalytic performance of the Cr- and Fe-based MPTBs catalysts towards OER including  $\eta_{\text{onset}}$  are different from those of Al-based MPTBs.

**Table S8.** Derived data of  $\eta_{\text{onset}}$  for OER

MPTB catalysts	<sup>b</sup> $\eta_{\text{onset}}$ (in mV vs. NHE)	
	Fresh	Used <sup>c</sup>
AlO5	136	102
AlO6	105	115
AlO7	4	45
AlN7	4	134
AlO8	15	93
AlO9	15	102
FeO7	196	263
FeO8	88	195
CrO7	76	181
CrO8	149	232

<sup>b</sup>Values of  $\eta_{\text{onset}}$  was determined through Equation S12 from LSV data shown in Fig. 3.

<sup>c</sup>After performing OER for 18 h at a constant potential of 1.51 V vs. NHE (Fig. 4a).

The determination of TOF values was carried out through the chronocoulometric measurements of charge ( $Q$ )-time ( $t$ ) responses of OER using different MPTBs as shown in Fig. S11.

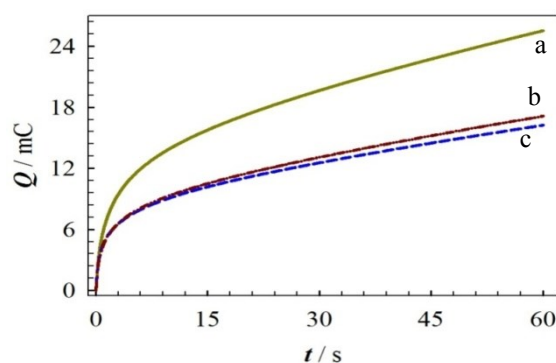


**Fig. S11.** Chronocoulometric measurement of OER at (a) AlO7, (b) FeO8 and (c) CrO7-modified graphite electrodes in 0.08 M H<sub>2</sub>SO<sub>4</sub> solution.

The different resistances associated with solution conductivities and electrode reactions such as solution resistance and charge-transfer resistance were determined by electrochemical impedance spectroscopic measurement of OER at AlO<sub>7</sub> modified electrode as shown in Fig. S12. The complex impedance data represent distorted semi-circle, which indicates the composite electrode material that consist of a mixture of ionically and electronically conducting phases with porous current collection layer.<sup>S18</sup> Negligible solution resistance of ca. 17.2  $\Omega$  and low charge-transfer resistance of ca. 37.8  $\Omega$  show the fast electron transfer rate due to highly accessible active sites that facilitated the OER.<sup>S19</sup>

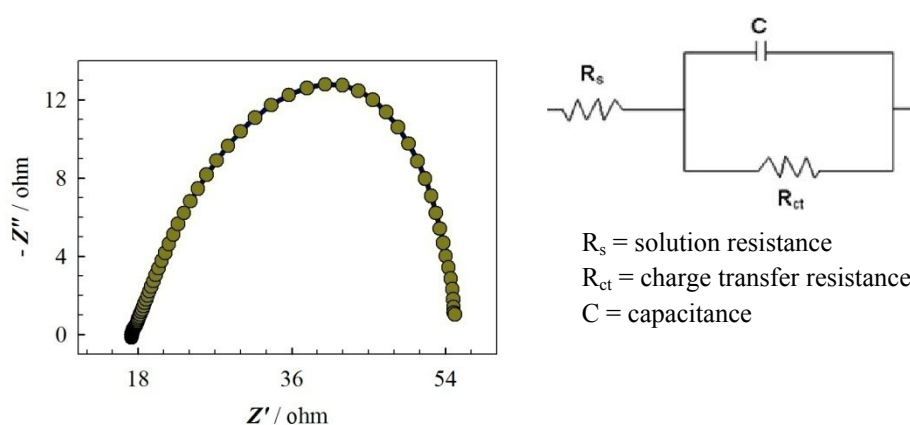


**Fig. S12** Electrochemical impedance spectrum of OER measured with AlO<sub>7</sub> using a *dc* potential of 1.81 V vs. NHE at a frequency region of 0.005 - 10<sup>5</sup> Hz and simplified Randles equivalent circuit<sup>S18</sup> employed for fitting.

## References

- S1. P. Roussel, O. Pérez, P. Labbé, *Acta Crystallogr. Sect. B Struct. Sci.* 2001, **57**, 603–632.
- S2. R. Romero Toledo, V. Ruiz Santoyo, C. D. Moncada Sánchez, M. Martínez Rosales, *Nov. Sci.* 2018, **10**, 83.
- S3. Y. Arai, D. L. Sparks, *J. Colloid Interface Sci.* 2001, **241**, 317–326.
- S4. M. Gotić, S. Musić, *J. Mol. Struct.* 2007, **834–836**, 445–453.
- S5. N. Daude, C. Gout, C. Jouanin, *Phys. Rev. B* 1977, **15**, 3229–3235.
- S6. N. Serpone, D. Lawless, R. Khairutdinov, *J. Phys. Chem.* 1995, **99**, 16646–16654.
- S7. Q. Chen, H. H. Cao, *Chinese Phys.* 2004, **13**, 2121–2124.
- S8. R. López, R. Gómez, *J. Sol-Gel Sci. Technol.* 2012, **61**, 1–7.
- S9. D. P. Joseph, C. Venkateswaran, *J. At. Mol. Opt. Phys.* 2011, **2011**, 1–7.

- S10. A. Tauc, J., Grigorovici, R. & Vancu, *Phys. Stat. Sol.* 1966, **15**, 627–637.
- S11. S. Sakhivel, M. C. Hidalgo, D. W. Bahnemann, S. U. Geissen, V. Murugesan, A. Vogelpohl, *Appl. Catal. B Environ.* 2006, **63**, 31–40.
- S12. G. Leftheriotis, S. Papaefthimiou, P. Yianoulis, A. Siokou, *Thin Solid Films* 2001, **384**, 298–306.
- S13. L. I. Granone, A. C. Ulpe, L. Robben, S. Klimke, M. Jahns, F. Renz, T. M. Gesing, T. Bredow, R. Dillert, D. W. Bahnemann, *Phys. Chem. Chem. Phys.* 2018, **20**, 28267–28278.
- S14. C. D. Wagner, W. M. Riggs, L. E. Davis, J. E. Moulder in *Handbook of X-ray Photoelectron Spectroscopy* (Eds.: G. E. Muilenberg) Perkin-Elmer Corporation, Minnesota, 1979, pp. 12–23.
- S15. J. D. Benck, T. R. Hellstern, J. Kibsgaard, P. Chakthranont, T. F. Jaramillo, *ACS Catal.* 2014, **4**, 3957–3971.
- S16. Y. Sun, S. Zhang, W. H. Zhang, Z. Y. Li, *Chinese J. Chem. Phys.* 2018, **31**, 485–491.
- S17. R. Lv, J. A. Robinson, R. E. Schaak, D. Sun, Y. Sun, T. E. Mallouk, M. Terrones, *Acc. Chem. Res.* 2015, **48**, 56–64.
- S18. N. Bonanos, B. C. H. Steele, E. P. Butler in *Impedance Spectroscopy: Theory, Experiment, and Applications* (Eds.: E. Barsoukov, J. R. Macdonald) John Wiley & Sons, Inc. Hoboken, 2018, pp. 175–224.
- S19. A. M. El-Sawy, I. M. Mosa, D. Su, C. J. Guild, S. Khalid, R. Joesten, J. F. Rusling, S. L. Suib, *Adv. Energy Mater.* 2016, **6**, DOI 10.1002/aenm.201501966.